01 Jul 2023

Kinetic Particle Simulations Of Plasma Charging At Lunar Craters Under Severe Conditions

David Lund

Xiaoming He
Missouri University of Science and Technology, hex@mst.edu

Daoru Frank Han
Missouri University of Science and Technology, handao@mst.edu

Recommended Citation

D. Lund et al., "Kinetic Particle Simulations Of Plasma Charging At Lunar Craters Under Severe Conditions," *Journal of Spacecraft and Rockets*, vol. 60, no. 4, pp. 1176 - 1187, American Institute of Aeronautics and Astronautics, Jul 2023.
The definitive version is available at https://doi.org/10.2514/1.A35622

JOURNAL OF SPACECRAFT AND ROCKETS
Vol. 60, No. 4, July–August 2023

Kinetic Particle Simulations of Plasma Charging at Lunar Craters Under Severe Conditions

David Lund,* Xiaoming He,† and Daoru Han‡
Missouri University of Science and Technology, Rolla, Missouri 65409

https://doi.org/10.2514/1.A35622

This paper presents fully kinetic particle simulations of plasma charging at lunar craters with the presence of lunar lander modules using the recently developed Parallel Immersed-Finite-Element Particle-in-Cell (PIFE-PIC) code. The computation model explicitly includes the lunar regolith layer on top of the lunar bedrock, taking into account the regolith layer thickness and permittivity as well as the lunar lander module in the simulation domain, resolving a nontrivial surface terrain or lunar lander configuration. Simulations were carried out to study the lunar surface and lunar lander module charging near craters at the lunar terminator region under mean and severe plasma environments. The lunar module's position is also investigated to see its effect on the plasma charging relative to the craters. Differential surface charging was clearly resolved by the simulations. For the charging of a lunar lander module made of conducting materials, the results show a near-uniform potential close to that of its surrounding environment and moderate levels of local electric fields. Additionally, the risks associated with charging and discharging increase significantly under a more severe plasma charging environment as shown in the severe plasma environment cases.

Nomenclature

n	=	number density
r	=	radius
T	=	temperature
v	=	velocity
λ_D	=	Debye length

Subscripts

d	=	drifting
t	=	thermal

I. Introduction

THIS paper considers the plasma charging near the lunar surface for future exploration missions, specifically, near lunar craters at the terminator region. Observations of the moon have found the potential of the sunlit surface is typically a few tens of volts positive with respect to ambient due to photoelectron emission, while the surface in shadow can be hundreds to thousands of volts negative due to the hot electron flux from ambient plasma which dominates the charging process [1–8]. Near the lunar polar regions, which are target destinations for planned Artemis missions, the rugged surface terrain generates localized plasma wakes and shadow regions that can lead to strong differential charging at the surface [9–11]. The localized plasma flowfield, the charged lunar surface, and the charged dust clouds are expected to have substantial influence on the charging of the lunar surface, landers/rovers/habitats, instruments, and astronauts on the lunar surface [12–14]. Hence, mitigating the lunar dust and threat of electrostatic discharge becomes a priority, and a thorough understanding with the ability to accurately predict plasma/surface/dust interactions near the lunar surface is vital for upcoming Artemis missions.

The lunar surface is covered by the lunar regolith layer, which separates the solid bedrock from the plasma environment. The regolith layer in most areas is about 4 to 20 m thick [15,16]. Over the years, there have been many modeling studies looking at plasma charging of the lunar surface and lunar dust grains [17–27] (cf. Refs. [28–30] for a more detailed literature review). A complete model of plasma charging on the lunar surface needs to explicitly take into account the properties of the regolith layer (such as its permittivity and layer thickness) and the lunar ground. Recently, Han et al. [28] presented a general approach of modeling plasma charging at the lunar surface including the lunar regolith layer as well as the lunar ground below the regolith layer. This approach integrated particle-in-cell (PIC) with a nonhomogeneous immersed-finite-element (IFE) field solver capable of resolving the charging of dielectric materials [31,32]. The main idea of IFE methods is to incorporate physical interface jump conditions in the design of local IFE functions [33]. In the past two decades, the IFE methods have been extensively studied for elliptic interface partial differential equation problems [34–42], parabolic interface problems [43,44], hyperbolic interface problems [45–47], Stokes interface problems [48,49], and so on. It has been shown that the IFE method can achieve optimal convergence on an interface-independent mesh with the number and location of the degrees-of-freedom isomorphic to the standard finite element methods on the same mesh [50–52]. The IFE functions have been used in various numerical frameworks such as the discontinuous Galerkin method [53–55], finite volume method [56–58], and nonconforming finite element method [59]. Over the past decades, the IFE method has been successfully used together with PIC in plasma particle simulations [60–65], including a nonhomogeneous IFE-PIC algorithm used in Ref. [28]. In the past few years, the IFE-PIC method has matured to successfully model plasma dynamics problems arising from many space applications, such as charging of lunar and asteroidal surfaces [66–71] and dust transport dynamics around small asteroids [72].

For problems of electrostatic plasma charging of materials (i.e., the topic of this study), the three-dimensional (3D) IFE-PIC model is capable of solving the electric field and charge deposition both inside and outside of irregularly shaped objects immersed in a plasma, which is unique among PIC-based charging models. The charging calculation from local charge deposition in the PIC approach also enables time-varying modeling of the charging process. In the work by Han et al. [28], two plasma charging problems were considered. The first problem considered lunar surface charging at the lunar terminator. The simulation model treated the lunar regolith layer as part of the simulation domain rather than as a boundary to the ambient

Presented as Paper 2020-1549 at the AIAA SciTech Forum 2020, Orlando FL, January 6–10, 2020 and Paper 2021-1434 at the AIAA SciTech Forum 2021, Virtual, January 11–15 and 19–21, 2021; received 12 November 2022; revision received 19 January 2023; accepted for publication 23 January 2023; published online 27 February 2023.

*Graduate Research Assistant, Department of Mechanical and Aerospace Engineering, 400 West 13th Street. Student Member AIAA.

†Associate Professor, Department of Mathematics and Statistics, 400 West 12th Street.

‡Assistant Professor, Department of Mechanical and Aerospace Engineering, 400 West 13th Street; handao@mst.edu. Senior Member AIAA.

plasma. Hence, it explicitly took into account the regolith layer permittivity and thickness. The floating potential of the regolith surface and the bedrock was calculated self-consistently from local charge deposition, and the electric field was resolved both in the ambient plasma and in the regolith layer. The second one considered the charging of a lunar outpost (LO) in a localized shadow region behind a hill at the lunar terminator. The simulation model treated the LO also as part of the simulation domain, and the LO charging was calculated self-consistently from local charge deposition. The results suggested that, near the lunar terminator, even under a very moderate plasma charging environment, substantial differential charging (when one region charges to a different potential than another) could develop. Lunar regolith, being dielectric, has high possibilities to experience differential charging at uneven places. Understanding the phenomenon of differential charging is critical because the chance for discharge and arcing becomes more prevalent for astronauts, their spacesuits, and equipment.

The IFE-PIC code package in Ref. [28] was serial, which has limited its applications to relatively small-sized problems with respect to practical interests, such as the charging of large lunar craters. Toward the goal of developing a massively scalable, first-principled-based, multiscale, multispecies modeling framework for complex plasma-surface interactions, Han et al. [29] and Lund et al. [30] developed the Parallel Immersed-Finite-Element Particle-in-Cell (PIFE-PIC) method with 3D domain decomposition using Message-Passing-Interface parallel computing architecture, where each subdomain is handled by an individual processor. In this paper, we use the most updated PIFE-PIC package [29,30] to conduct fully kinetic simulations of plasma charging at lunar craters (some of which include lunar lander modules) under mean and severe magnetosheath plasma environments.

The rest of this paper is organized as follows. Section III presents the simulation setup for the lunar crater and the lunar lander module charging calculations. Section IV discusses the simulation results. Finally, Sec. V contains a summary and conclusion.

II. Simulation Setup

In this work, we follow the simulation setup procedure of our earlier work using serial IFE-PIC as in Ref. [28], with the new parallel code suite PIFE-PIC as well as more realistic geometric models of lunar craters.

A. Plasma Environment

The plasma species are chosen to include the ambient electrons and ions (depending on the location of the moon in its orbit) and photoelectron parameters at the lunar surface in the magnetosheath day side environment. The environment's parameters were retrieved from NASA's Cross-Program Design Specification for Natural Environments (DSNE) document [73]. The plasma conditions listed in the DSNE document include the mean, the 95% range, the 99.7% range, and the maximum range of the observed environments derived from the THEMIS-ARTEMIS data in the years 2012 through 2018. This study includes the mean plasma conditions in the magnetosheath day side environment, shown in Table 1, as well as the 99.7% range of the observed plasma conditions, which we will refer to as the *99.7%* plasma condition, in the magnetosheath day side environment, shown in Table 2.

In PIFE-PIC, all dimensions are normalized (dimensionless) using the photoelectron parameters at a 90 deg sun elevation angle as the normalization reference for each respective environment and plasma condition. All the simulation results presented here are for a 5 deg sun elevation angle representing the lunar terminator region. When setting up the cases for 5 deg sun elevation angles, solar wind species would break their velocity components into horizontal and vertical directions using the flow direction angle [i.e., a factor of cos(5 deg)]. For photoelectrons generated locally on the surface, their numbers were also scaled similarly based on the local sun elevation angle (using the inner product of the sun vector and the local surface normal vector).

Table 1 DSNE mean magnetosheath dayside plasma conditions and photoelectron (at 90 deg sun elevation angle) parameters in the magnetosheath day side plasma environment (N/A denotes not applicable)

Plasma species	Number density n, cm^{-3}	Drifting velocity v_d, $\times 10^7$ cm/s	Thermal velocity v_t, $\times 10^7$ cm/s	Temperature T, eV	Debye length λ_D, m
Electron	9.5	3.5	17.79	18	10.24
Ion	9.5	3.5	0.95	94	N/A
Photoelectron	100	N/A	6.22	2.2	1.10

Table 2 DSNE 99.7% magnetosheath dayside plasma conditions and photoelectron (at 90 deg sun elevation angle) parameters in the magnetosheath day side plasma environment (N/A denotes not applicable)

Plasma species	Number density n, cm^{-3}	Drifting velocity v_d, $\times 10^7$ cm/s	Thermal velocity v_t, $\times 10^7$ cm/s	Temperature T, eV	Debye length λ_D, m
Electron	1.3	6.4	56.25	180	87.57
Ion	1.3	6.4	3.25	1100	N/A
Photoelectron	100	N/A	6.22	2.2	1.10

B. Computation Domain and Boundary Conditions

The computation domain has $120 \times 40 \times 60$ PIC cells for the simulations with the mean plasma conditions and has $200 \times 125 \times 350$ PIC cells for the 99.7% plasma condition because the more extreme environment has a larger Debye length, resulting in the need of a larger domain size. In physical units, the domain size is approximately 132 by 44 by 66 m for the mean plasma conditions and 220 by 137.5 by 385 m for the 99.7% plasma condition. At the $Z_{\min}$ boundary, the simulation domain includes a layer of conducting bedrock with a thickness of 5.23 m. On top of the bedrock is a layer of dielectric regolith with a thickness of 5.5 m. The lunar bedrock layer and the regolith layer have a relative permitivitty of 4. A Dirichlet boundary condition of zero potential is applied at the $Z_{\max}$ boundary, whereas a Neumann boundary condition for the zero electric field is applied on the five other domain boundaries.

Particles representing ions and electrons are preloaded and injected into the domain with an angle of 5 deg toward the surface in the X-Z plane. Particles representing photoelectrons are generated at the sunlit regions according to the local sunlight index. At the global $X_{\min}$, $X_{\max}$, $Y_{\max}$, and $Z_{\max}$ domain boundaries, ambient solar wind particles are injected, and particles leaving these domain boundaries are removed from the simulation domain. Particles hitting the global $Y_{\min}$ boundary are reflected due to symmetry. Particles hitting the lunar surface are collected, and their charges are accumulated to calculate surface charging. A diagram of the computational domain and boundary conditions are shown in Fig. 1.

C. Lunar Crater Geometry

In PIFE-PIC, arbitrary geometries for surface topographies are defined and produced through an algebraic equation in the form of $z = z(x, y)$. These arbitrary geometries need to be accurate enough to mimic realistic surface topographies. This is done through the study of morphometry, which is the process of measuring land-form shapes and dimensions. From a large database of detailed measurements of lunar imagery, it has been made possible to represent the different geometrical characteristics of lunar craters including the rim width, rim height, rim diameter, and crater depth [74]. The different dimensions of the craters can be calculated by only knowing the diameter of the crater from the equation of the form $y = a \times D^b$, where y is a given crater characteristic (crater depth, rim height, etc.), D is the diameter of the crater, and a and b are various constants [74]. The specific diameter of a real lunar crater can be measured from NASA's Jet Propulsion Laboratory's website, Moon Trek [75].

The shape of the lunar crater considered in this study is defined by the equation of a circle, Eq. (1), and a series of flat lines and cosine curves, Eqs. (2–5). The center position of the crater is defined by Eq. (1) at the (x, y) location of (40,0) in the domain for the mean

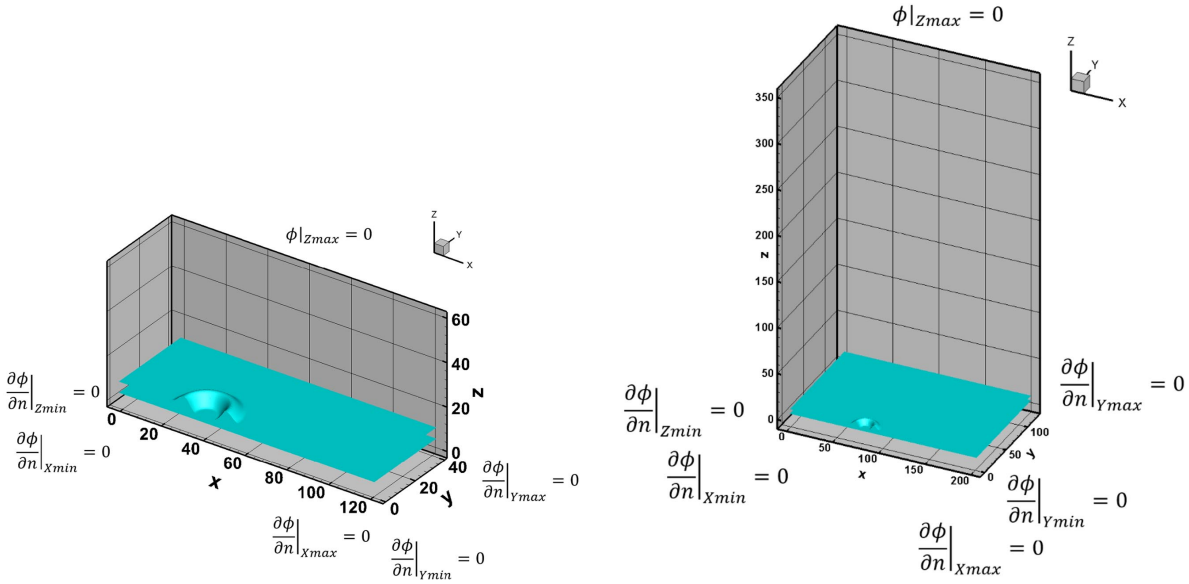

a) Mean magnetosheath day side plasma environment **b) 99.7% magnetosheath day side plasma environment**

Fig. 1 Computational domain and boundary conditions.

plasma condition case (normalized coordinates). This causes only half the crater to be generated, so the remaining half of the crater is generated by mirroring the domain over the X-Z plane. Equation (2) is used to generate the inner floor region inside the crater for the range of ($r \leq 4.5$). Equation (3) is used to generate the inner, uphill side of the rim for the range of ($4.5 < r \leq 10.0$). Equation (4) is used to generate the outer, downhill side of the rim for the range of ($10.0 < r \leq 16.0$). Equation (5) is used to generate the flat lunar surface for the range of ($r > 16.0$),

$$r = \sqrt{(x-40)^2 + y^2} \tag{1}$$

$$z = -2.05 \tag{2}$$

$$z = 2.8 \times \left(1 - \cos\left(\frac{r-4.5}{5.5} \times \pi\right)\right) - 2.05 \tag{3}$$

$$z = 1.775 \times \left(1 + \cos\left(\frac{r-10}{6} \times \pi\right)\right) \tag{4}$$

$$z = 0 \tag{5}$$

Finally, Eq. (6) offsets Eqs. (2–5) to fit properly within the simulation domain,

$$z = z + 9.75 \tag{6}$$

In physical units, the lunar crater has a height of approximately 3.91 m and a depth of 2.26 m (both with respect to the flat surface). Also, the lunar crater has an outer radius of 17.6 m, a rim radius of 11 m, and an inner radius of 4.95 m.

III. Results and Discussion

PIFE-PIC has three levels of iterations (loops): the main PIC loop, the domain decomposition method (DDM) loop, and the matrix solver preconditioned conjugate gradient (PCG) loop. More details of the PIFE-PIC framework, including parallel efficiency tests for strong and weak scaling, are presented in Refs. [29,30].

For a typical run, the maximum number of the PCG field solver iterations was set to 1000 with a tolerance of 1×10^{-6} for absolute residue. The maximum number of initial DDM iterations (solving the initial electrostatic field before the main PIC loop starts) was set to 2000, and the maximum number of DDM iterations at each PIC iteration step was set to 200 with a tolerance of 1×10^{-4} for relative error. The simulations were set to run 10,000 PIC steps for the cases with the mean plasma conditions and 25,000 PIC steps for the 99.7% plasma condition on the Foundry cluster provided by the Center of High-Performance Computing Research at Missouri University of Science and Technology. The computing nodes are configured with Dell C6525 nodes, each having four node chassis with each node containing dual 32-core Advanced Micro Devices (AMD) EPYC Rome 7452 CPUs with 256 GB Double Data Rate Fourth Generation (DDR4) RAM and six 480 GB Solid-State Drive (SSD) drives in Redundant Array of Independent Disks (RAID 0). A typical run took nine to ten wall-clock hours for the mean plasma conditions in the magnetosheath day side environment running on 288 CPUs with a domain decomposition configuration of $12 \times 4 \times 6$ and a normalized time step size of 0.02. A typical run for the 99.7% plasma condition in the magnetosheath day side environment took approximately 60 to 66 wall-clock hours to finish on 560 CPUs with a domain decomposition configuration of $8 \times 5 \times 14$ and a normalized time step size of 0.02. The total physical time of the simulation for the mean magnetosheath case was 0.0022 s, and the total physical time for the 99.7% magnetosheath case was 0.0056 s.

In the following figures (Figs. 2–7), the distance is normalized by $\lambda_D = 1.10$ m, the density is normalized by $n = 100$ cm^{-3}, the potential is normalized by $T = 2.2$ eV, and the electric field is normalized by 2.0 V/m. Section IV is broken down into two main subsections: the first subsection includes regolith surface charging at the lunar terminator with only a crater present, and the second subsection includes regolith surface charging at the lunar terminator with a crater as well as a lunar lander module present in multiple locations. Each subsection considers surface charging in the two different magnetosheath plasma environments.

A. Regolith Surface Charging at Lunar Terminator Crater

As the moon orbits the earth, it is exposed to several different plasma environments. About three-quarters of its time the moon spends in the solar wind plasma environment, but the remainder is within the terrestrial magnetosheath and geomagnetic tail. These regions contain denser/more energetic plasma [76]. We first consider surface charging for a lunar crater in the two different plasma environments: mean plasma conditions in the magnetosheath day side environment and the 99.7% plasma condition in the magnetosheath day side environment shown in Figs. 2 and 3, respectively.

Figure 2a shows the normalized ion density contours, Fig. 2b shows the normalized electron density contours, and Fig. 2c shows the normalized photoelectron density contours. Figure 2d shows the normalized potential contours near the lunar regolith surface.

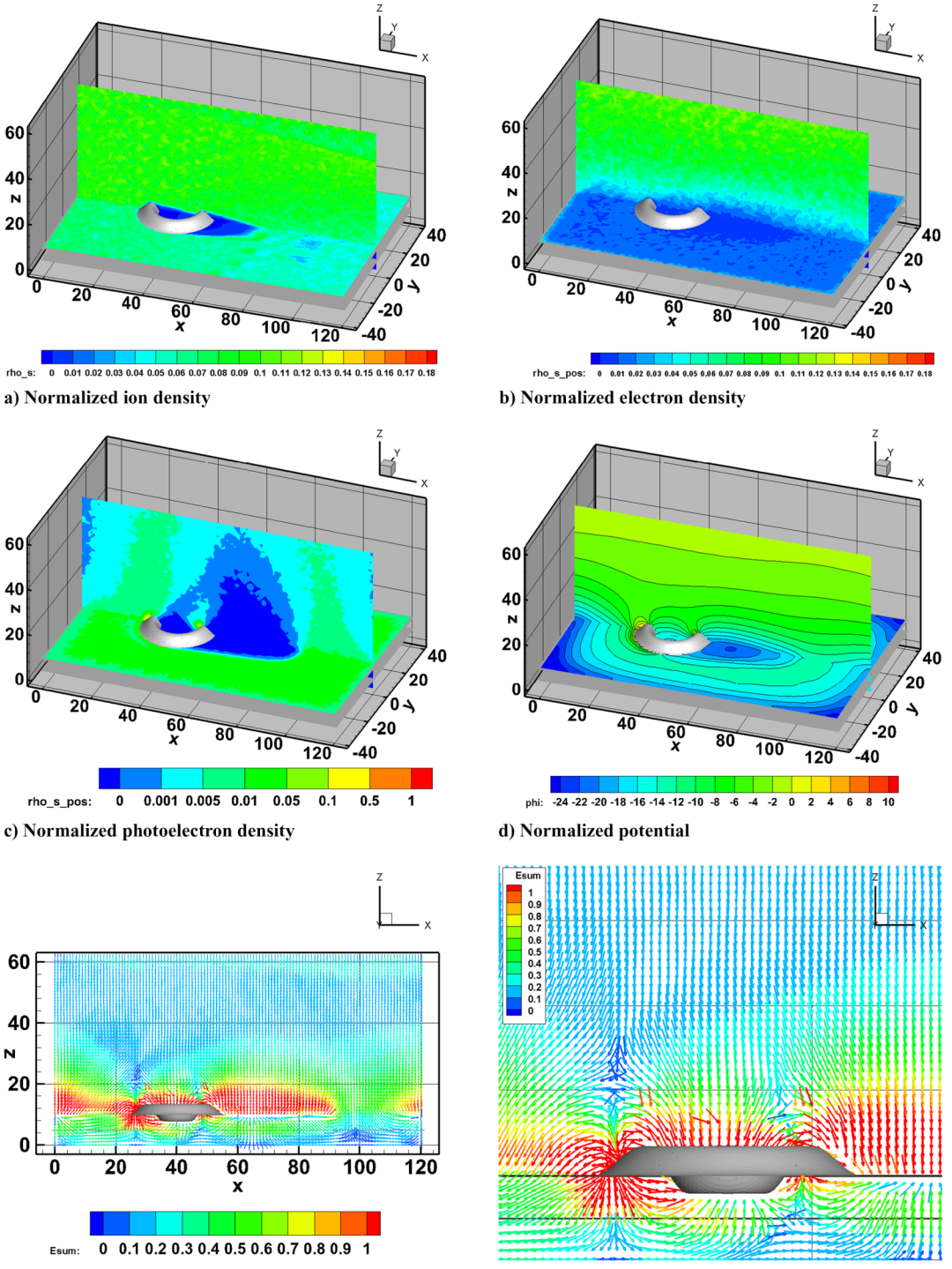

a) Normalized ion density

b) Normalized electron density

c) Normalized photoelectron density

d) Normalized potential

e) Electric field vectors in *X-Z* plane

f) Electric field vectors in *X-Z* plane (zoomed in)

Fig. 2 Plasma charging at the lunar crater with mean plasma conditions in the magnetosheath day side environment.

The results clearly show a localized plasma wake formed by the lunar crater. The plasma wake region can be seen inside the crater around the left wall as well as regions behind the crater. The physics of the localized plasma wake formation can be described by the expansion of collisionless, mesothermal plasma flowing over an object [77]. As the plasma expands into the wake region, the electric potential, ion density, electron density, and photoelectron density decrease.

For the magnetosheath day side in the mean plasma environment (Fig. 2), the surface potential in front of the crater is approximately 4.4 V, inside the crater on the left wall is approximately −30.8 V, inside the crater on the right wall is approximately −6.6 V, and behind the crater is approximately −52.8 V. The crater also generates a plasma wake region extending to about 26.4 m behind the outer right wall as well as a small plasma wake region within the crater. The areas where the crater walls block the sunlight are the most negative due to a lack of ion collection and photoelectron emission. The surface potential is very negative in this environment (specifically in the wake region but generally everywhere). This can most likely be attributed to the higher density and temperatures of the ion and electron particles.

The simulation model also resolves the electric field inside the regolith layer. Figure 2e shows the electric field vectors on the lunar surface near the crater region, and Fig. 2f shows a zoomed-in view of the electric field vectors around the lunar crater. The electric field at the regolith surface is nonzero due to charge accumulation. For the magnetosheath day side in the mean plasma environment, the electric

field's magnitude is consistently 2.0 V/m and extends about 22 m over the plasma wake region as well as all the way upstream of the crater. The electric field magnitude decreases to 0 V/m at about 44 m above the surface. The electric field inside the regolith layer is controlled by the net charge deposited at the regolith surface as well as the capacitance of the regolith layer. The capacitance of the regolith layer can be sensitively influenced by the properties of the regolith. It is noted that the values calculated assume the regolith can be modeled by a dielectric layer with a thickness of about 5.5 m and a relative permittivity of 4. Previous work [28] showed the surface potentials are mainly driven by the current balance condition and are insensitive to the thickness of the regolith layer.

One additional case was run for an extreme plasma charging environment because the charging risk for the lunar crater is expected to be significantly higher under a more severe plasma charging environment. Results for plasma charging at the lunar crater within the 99.7% plasma condition in the magnetosheath day side environment are shown in Fig. 3. The surface potential behind the crater is approximately −275 V. The crater generates a plasma wake region extending to about 45 m behind the outer right wall. Figure 3e shows

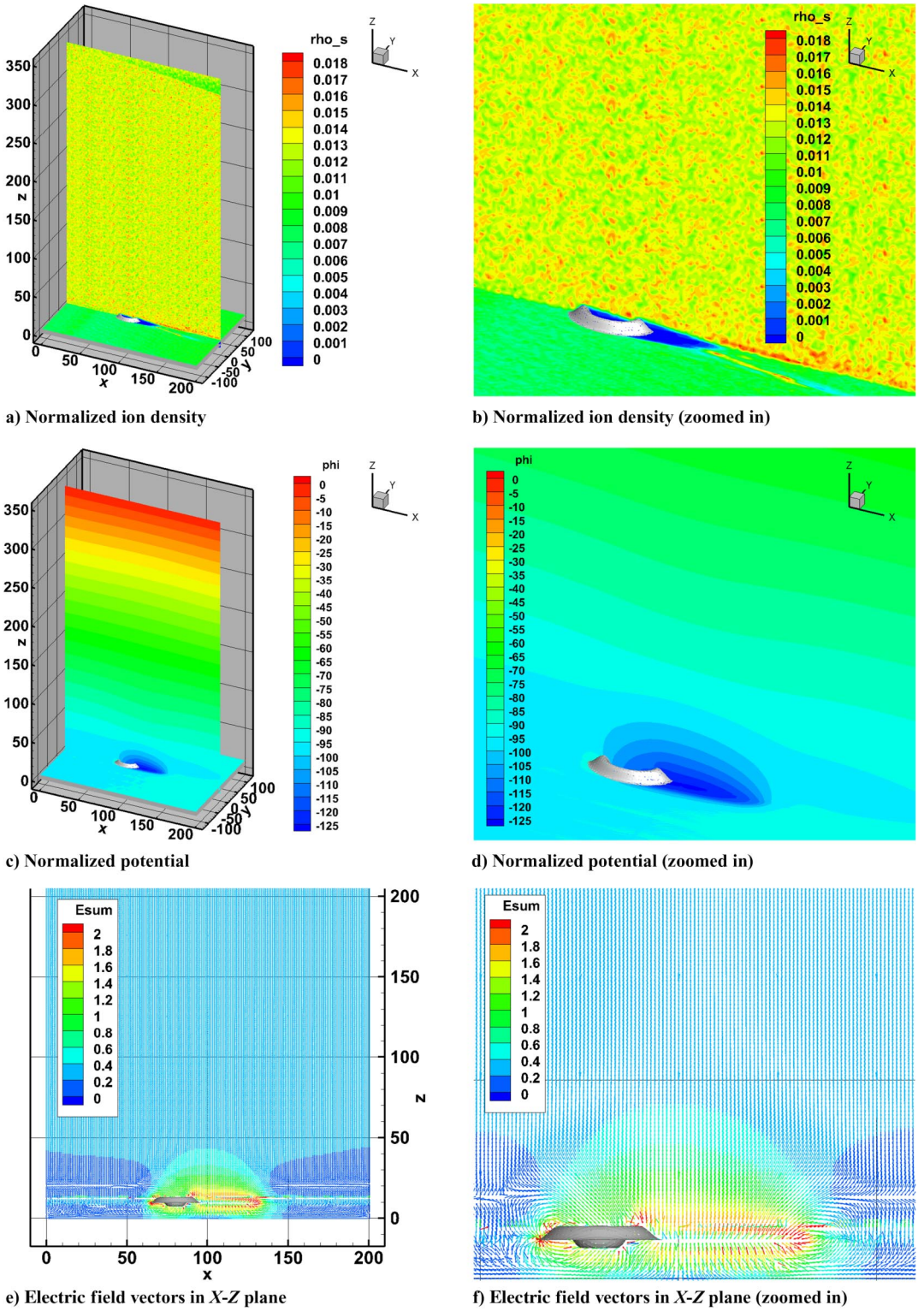

a) Normalized ion density

b) Normalized ion density (zoomed in)

c) Normalized potential

d) Normalized potential (zoomed in)

e) Electric field vectors in *X-Z* plane

f) Electric field vectors in *X-Z* plane (zoomed in)

Fig. 3 Plasma charging at the lunar crater with 99.7% plasma condition in the magnetosheath day side environment (E = Electric).

the electric field vectors on the lunar surface, and Fig. 3f shows a zoomed-in view of the electric field vectors around the lunar crater. The electric field magnitude around the lunar crater and in the plasma wake region is about 3.0 to 4.0 V/m for this extreme environment. The strength of the electric field does not extend upstream from the lunar crater and is contained around the crater and the plasma wake region.

In an earlier study conducted by Halekas et al. [76], lunar surface charging during solar energetic particle events were observed. The authors studied 11 different time periods where the Lunar Prospector Electron Reflectometer recognized large negative surface potentials. Although their focus was on the solar wind plasma environments, their characterization of surface charging between the 11 events leads to correlations of parameters that can be extended to other plasma environments. For the majority of the time periods (9 out of 11), the negative surface potential of the lunar surface has a direct correlation with the thermal electron temperature and the ratio of the energetic electron flux to the energetic proton flux. Referring back to Tables 1 and 2, the thermal electron temperature for the 99.7% plasma condition (180 eV) is ten times larger than the mean plasma conditions (18 eV) in the magnetosheath day side environment. Looking at the results of our two simulations, the surface potential increases from −52.8 to −275 V in the plasma wake behind the crater (from the mean to the 99.7% plasma condition), which corresponds and strengthens the expectations that the thermal electron temperature plays a role in altering the surface potential.

B. Lunar Lander Module Charging at Lunar Terminator

Charging was not considered a serious risk during the Apollo era because the Apollo astronauts always stayed in the sunlit region. Future lunar missions may require exploration activities in more complex lunar terrain. In this section, we further consider the charging of a small lunar lander module made with conductive materials (relative permittivity of 100, which is 25 times larger than the lunar regolith) positioned slightly above the lunar surface at two different positions:

1) In position 1 (Figs. 4 and 5), the lunar lander module is 27.5 m in front of the lunar crater's center and 2.2 m over the lunar surface. This position represents a landing scenario *upstream* from the crater.

2) In position 2 (Figs. 6 and 7), the lunar lander module is 27.5 m behind the lunar crater's center and 2.2 m over the lunar surface. This position represents a landing scenario *downstream* from the crater.

For both lunar lander module positions, the surface charging was considered in the same two plasma environments as in the crater-only case. The small lunar lander module is represented by a sphere with a radius of 1.65 m. Photoelectron emission characteristics of the lunar lander is assumed to be the same as the lunar surface. It is noted here that this assumption most likely will not make a significant difference because the size of the conductive lunar lander is small compared to the dielectric lunar surface. Additionally, according to experimental data, the photoemission yield of aluminum is slightly lower than JSC-1A (a lunar simulant), 4.2 for aluminum, and 5.8 for JSC-1A [78]. Future work will look more into this effect.

1. *Position 1: Lunar Lander Module Upstream from Crater*

Figure 4 shows the normalized ion density contours, the normalized potential contours, the electric field vectors on the lunar surface near the crater region, and a zoomed-in view of the electric field vectors around the lunar crater and lunar lander module in position 1 for the magnetosheath day side in the mean plasma environment.

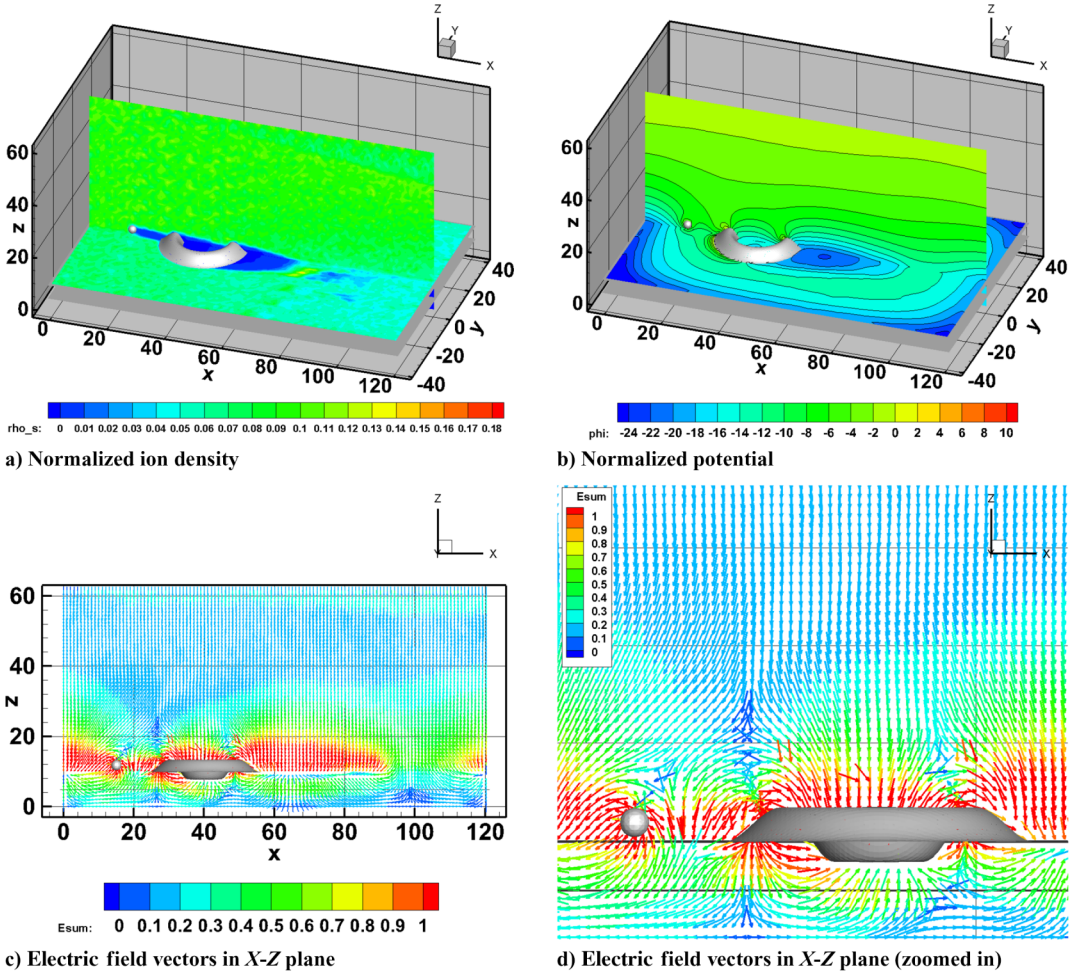

a) Normalized ion density

b) Normalized potential

c) Electric field vectors in *X-Z* plane

d) Electric field vectors in *X-Z* plane (zoomed in)

Fig. 4 Plasma charging at the lunar crater with the lunar lander module in position 1 (upstream from the crater) with mean plasma conditions in the magnetosheath day side environment.

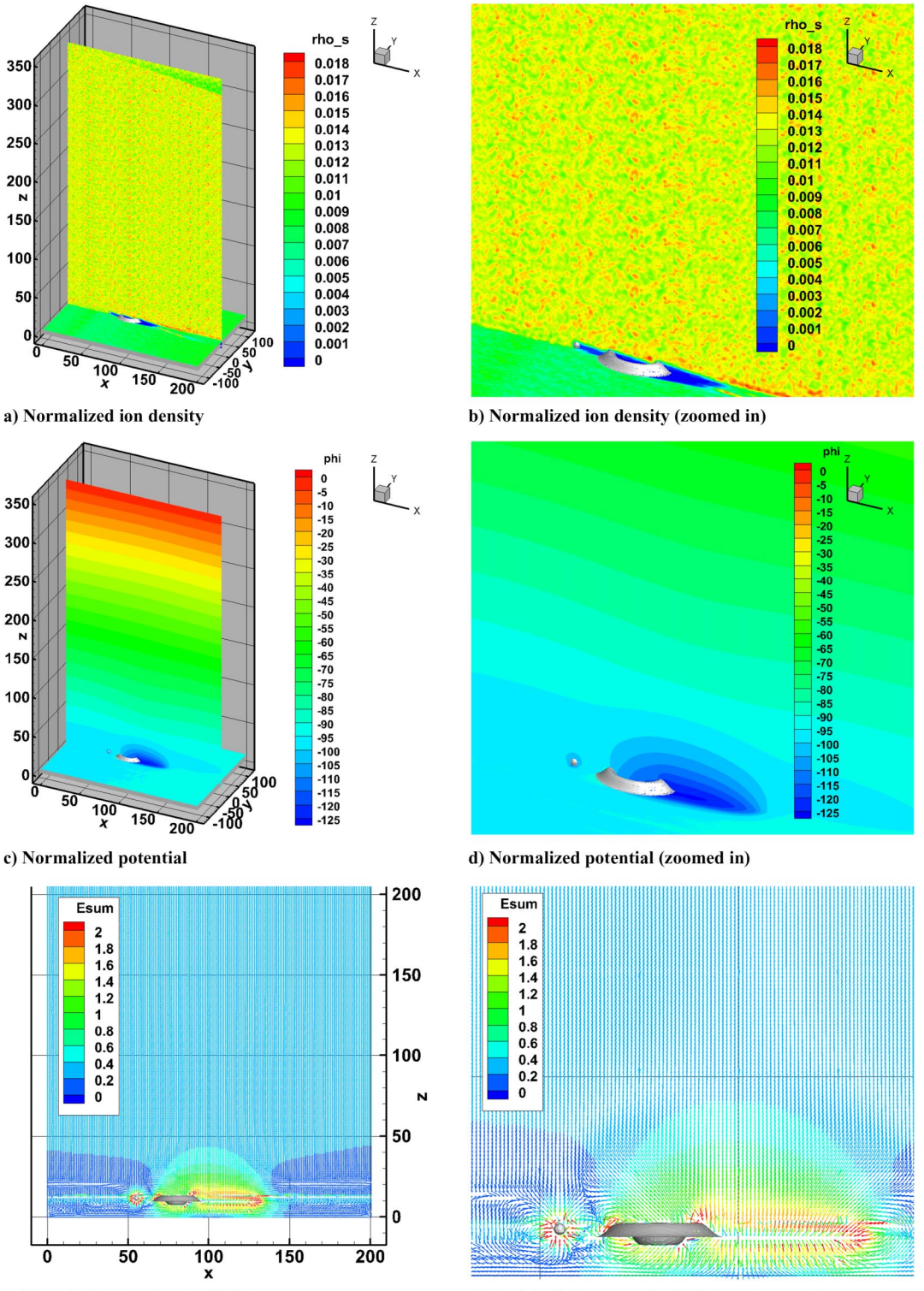

Fig. 5 Plasma charging at the lunar crater with the lunar lander module in position 1 (upstream from the crater) with 99.7% plasma condition in the magnetosheath day side environment.

Figure 4b shows the normalized potential contours near the lunar regolith surface.

For the magnetosheath day side in the mean plasma environment, the surface potential in front of the crater is approximately −17.6 V. This is different from the surface potential in front of the crater for the crater-only case, as that potential was 4.4 V. This can most likely be attributed to the lunar lander module blocking ions from reaching the crater, as shown in Fig. 4a, and a lower density of photoelectrons due to the lack of photoemission on the crater. Figure 4b shows the lunar lander module has a potential of about −13.2 V, which is about the same as the environment it is positioned in.

Figure 4c shows the electric field vectors on the lunar surface, and Fig. 4d shows a zoomed-in view of the electric field vectors around the lunar crater and lunar lander module. The electric field magnitude around the lunar crater, lunar lander module, and in the plasma wake region is once again consistently 2.0 V/m for the mean magnetosheath day side environment. The mean magnetosheath day side electric field's strength extends about 22 m and reaches 0 V/m at about 44 m above the surface. Also, the electric

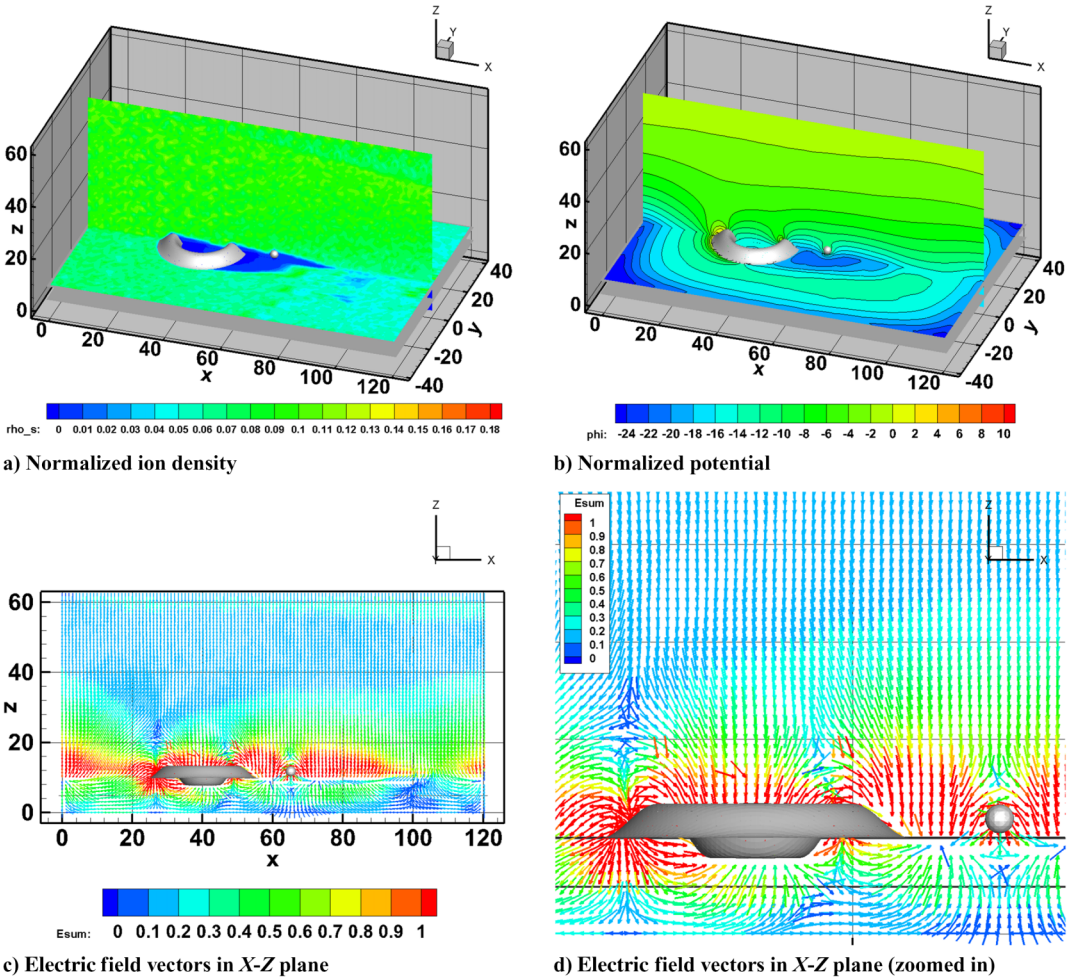

Fig. 6 Plasma charging at the lunar crater with the lunar lander module in position 2 (downstream from the crater) with mean plasma condition in the magnetosheath day side environment.

field can be seen as having an influence all the way to the front of the simulation domain.

Results for plasma charging at the lunar crater with the lunar lander module in position 1 within 99.7% plasma condition in the magnetosheath day side environment are shown in Fig. 5. The surface potential behind the crater is approximately −275 V. Figure 5c shows the lunar lander module also has a potential of about −275 V, which is about the same as the environment it is positioned in. The crater generates a plasma wake region extending to about 45 m behind the outer right wall. Figure 5e shows the electric field vectors on the lunar surface, and Fig. 5f shows a zoomed-in view of the electric field vectors around the lunar crater and lunar lander module. The electric field magnitude around the lunar crater, lunar lander module, and in the plasma wake region is about 3.0 to 4.0 V/m for this extreme environment. Although this time, the strength of the electric field does not extend much upstream the lunar crater and is contained around the crater, the lunar lander module, and the plasma wake region.

2. *Position 2: Lunar Lander Module Downstream from Crater*

Figure 6 shows the normalized ion density contours, the normalized potential contours, the electric field vectors on the lunar surface near the crater region, and a zoomed-in view of the electric field vectors around the lunar crater and lunar lander module in position 2 for the magnetosheath day side in the mean plasma environment. Figure 6b shows the normalized potential contours near the lunar regolith surface.

For the magnetosheath day side in the mean plasma environment, the surface potential behind the crater is approximately −52.8 V. This is the same surface potential behind the crater for the crater-only case. Once again, this similarity can most likely be attributed to the lunar lander module not blocking any ions or illumination. Figure 6b shows the lunar lander module has a potential of about −30.8 V on top of it and about −39.6 V underneath it. Both surface potentials (on top and bottom of the lunar lander module) are similar to their surroundings, but the surrounding potential around the module is different because the potential gradient changes over a short distance due to the large negative plasma wake behind the crater. Similarly to the crater-only case and the position 1 lunar lander module case, the mean magnetosheath day side environment has an overall very negative surface potential, illustrating the large potential difference the moon can go through as it navigates through its orbit.

Figure 6c shows the electric field vectors on the lunar surface, and Fig. 6d shows a zoomed-in view of the electric field vectors around the lunar crater and lunar lander module. The electric field magnitude around the lunar crater, lunar lander module, and in the plasma wake region is once again consistently 2.0 V/m for the magnetosheath day side environment. The same trends occur here that were discussed in the position 1 subsection.

Results for plasma charging at the lunar crater with the lunar lander module in position 2 within 99.7% plasma condition in the magnetosheath day side environment are shown in Fig. 7. The surface potential behind the crater is approximately −275 V. Figure 7c shows the lunar lander module also has a potential of about −275 V, which is about the same as the environment it is positioned in. The crater generates a plasma wake region extending to about 45 m behind the outer right wall. Figure 7e shows the electric field vectors on the lunar surface, and Fig. 7f shows a zoomed-in view of the electric field vectors around the lunar crater and lunar lander module. The electric field magnitude around the lunar crater, lunar lander module, and in

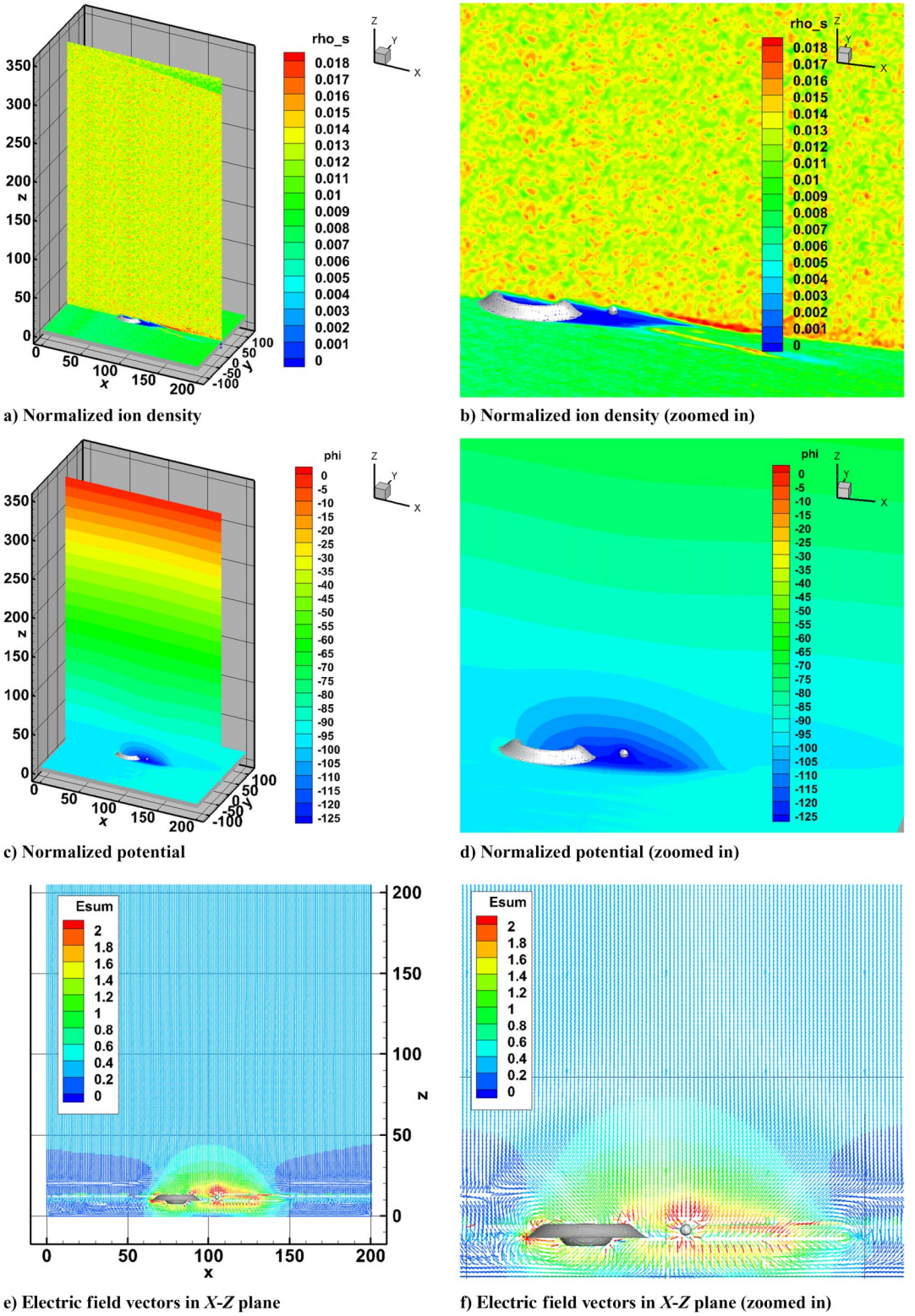

a) Normalized ion density

b) Normalized ion density (zoomed in)

c) Normalized potential

d) Normalized potential (zoomed in)

e) Electric field vectors in *X-Z* plane

f) Electric field vectors in *X-Z* plane (zoomed in)

Fig. 7 Plasma charging at the lunar crater with the lunar lander module in position 2 (downstream from the crater) with 99.7% plasma condition in the magnetosheath day side environment.

the plasma wake region is about 3.0 to 4.0 V/m for this extreme environment. Once again, the strength of the electric field does not extend upstream the lunar crater and is contained around the crater and the plasma wake region. It is also noted that the electric field surrounding the lunar lander module is more uniformly 4.0 V/m compared to the rest of the wake region.

Compared to the results shown in Sec. IV.A (crater only), the disturbances from the lunar lander module both upstream and downstream from the crater on the plasma field are obvious and will need to be taken into account in the modeling of dust interactions around the lunar lander module, especially when the lunar lander module is upstream from the crater because its presence blocks the ions and solar illumination, which significantly alters the surface charge of the lunar crater's rim. Also, because the material of the lunar lander module is modeled as a conductor, the presence and charging of the lunar lander module caused by both electron and ion bombardment as well as photoelectron emission develops nearly uniform charging between the lunar lander module and its surroundings.

IV. Conclusions

This paper presents fully kinetic numerical simulations of plasma charging at lunar craters (some of which include lunar lander modules) using the recently developed and massively parallel PIFE-PIC code. The computation model explicitly includes the lunar regolith layer, the lunar bedrock, and the lunar lander module as part of the simulation. Surface charging is calculated directly from the local charge deposition, and the electric field is obtained both inside the object and in the plasma.

Two applications are considered in this paper. The first considers regolith surface charging around a small crater at the lunar terminator. The results clearly show the differential charging of the lunar surface and strengthens the expectations that the thermal electron temperature plays a role in altering the surface potential. The second application considers the charging of a lunar lander module in two different positions (upstream and downstream from the crater) representing different landing locations. For all three cases (crater only, lunar lander module in position 1, and lunar lander module in position 2), two plasma environments retrieved from NASA's DSNE document were considered: mean plasma conditions in the magnetosheath day side environment as well as the 99.7% plasma condition in the magnetosheath day side environment. These cases are vital to the understanding of the surface charging of lunar craters and lunar lander modules in different plasma charging environments throughout the moon's orbit and how the landing positions of lunar modules can affect their surface charging and the charging of the surrounding lunar surface. The key conclusions here are that the near-uniform potential on the lunar lander module becomes close to that of its environment and the lunar lander module only significantly changes the charging of the lunar surface/crater when it is blocking ions and illumination. When the lunar lander module is downstream from the crater, its influence on the surface charging is negligible.

For the mean plasma conditions and the small lunar crater considered here, the results only show moderate charging. However, the surface charging for the magnetosheath day side plasma environment was negative and had an influential electric field surrounding the crater and extending far upstream.

Additionally, the risks associated with charging and discharging increase significantly under a more severe plasma charging environment as shown in the 99.7% plasma condition in the magnetosheath day side environment. This plasma environment was so severe that the surface potential for all three cases was similar, regardless of the presence of the lunar lander module or its landing position.

Acknowledgments

This work was partially supported by a NASA Space Technology Graduate Research Opportunity (D. L.), NASA-Missouri Space Grant Consortium through NASA-Experimental Program to Stimulate Competitive Research (EPSCoR)-Missouri (X. H. and D. H.) and graduate scholarships (D. L.), NASA Physical Sciences Informatics program (D. L. and D. H.), and the National Science Foundation through grants DMS-2111039 (X. H. and D. H.) and CBET-2132655 (D. H.). The simulations presented here were performed with computing resources provided by the Center for High Performance Computing Research at Missouri University of Science and Technology through National Science Foundation grant OAC-1919789.

References

[1] Reasoner, D. L., and Burke, W. J., "Characteristics of the Lunar Photoelectron Layer in the Geomagnetic Tail," *Journal of Geophysical Research*, Vol. 77, No. 34, 1972, pp. 6671–6687. https://doi.org/10.1029/JA077i034p06671

[2] Willis, R., Anderegg, M., Feuerbacher, B., and Fitton, B., "Photoemission and Secondary Electron Emission from Lunar Surface Material," *Photon and Particle Interactions with Surfaces in Space*, edited by R. Grard, Vol. 37, Astrophysics and Space Science Library, Springer–Verlag, Dordrecht, The Netherlands, 1973, pp. 389–401. https://doi.org/10.1007/978-94-010-2647-5_25

[3] Berg, O. E., Richardson, F. F., and Burton, H., "Apollo 17 Preliminary Science Report," NASA SP-330, 1973.

[4] Freeman, J. W., and Ibrahim, M., "Lunar Electric Fields, Surface Potential and Associated Plasma Sheaths," *Moon*, Vol. 14, No. 1, 1975, pp. 103–114. https://doi.org/10.1007/BF00562976

[5] Stubbs, T. J., Halekas, J. S., Farrell, W. M., and Vondrak, R. R., "Lunar Surface Charging: A Global Perspective Using Lunar Prospector Data," *Workshop on Dust in Planetary Systems (ESA SP-643)*, edited by H. Krueger, and A. Graps, European Space Agency (ESA), Paris, France, 2005, pp. 181–184.

[6] Halekas, J. S., Delory, G. T., Brain, D. A., Lin, R. P., Fillingim, M. O., Lee, C. O., Mewaldt, R. A., Stubbs, T. J., Farrell, W. M., and Hudson, M. K., "Extreme Lunar Surface Charging During Solar Energetic Particle Events," *Geophysical Research Letters*, Vol. 34, No. 2, 2007, Paper L02111. https://doi.org/10.1029/2006GL028517

[7] Halekas, J. S., Delory, G. T., Lin, R. P., Stubbs, T. J., and Farrell, W. M., "Lunar Prospector Observations of the Electrostatic Potential of the Lunar Surface and Its Response to Incident Currents," *Journal of Geophysical Research*, Vol. 113, No. A9, 2008, Paper A09102. https://doi.org/10.1029/2008JA013194

[8] Halekas, J. S., Saito, Y., Delory, G. T., and Farrell, W. M., "New Views of the Lunar Plasma Environment," *Planetary and Space Science*, Vol. 59, No. 14, 2011, pp. 1681–1694. https://doi.org/10.1016/j.pss.2010.08.011

[9] Berg, O. E., "A Lunar Terminator Configuration," *Earth and Planetary Science Letters*, Vol. 39, No. 3, 1978, pp. 377–381. https://doi.org/10.1016/0012-821X(78)90025-0

[10] Wang, J., He, X., and Cao, Y., "Modeling Electrostatic Levitation of Dust Particles on Lunar Surface," *IEEE Transactions on Plasma Science*, Vol. 36, No. 5, 2008, pp. 2459–2466. https://doi.org/10.1109/TPS.2008.2003016

[11] Poppe, A. R., Piquette, M., Likhanskii, A., and Horányi, M., "The Effect of Surface Topography on the Lunar Photoelectron Sheath and Electrostatic Dust Transport," *Icarus*, Vol. 221, No. 1, 2012, pp. 135–146.

[12] Hess, S., Sarrailh, P., Matéo-Vélez, J.-C., Jeanty-Buard, B., Cipriani, F., Forest, J., Hilgers, A., Honary, F., Thiebault, B., Marple, S., and Rodgers, D., "New SPIS Capabilities to Simulate Dust Electrostatic Charging, Transport, and Contamination of Lunar Probes," *IEEE Transactions on Plasma Science*, Vol. 43, No. 9, 2015, pp. 2799–2807. https://doi.org/10.1109/TPS.2015.2446199

[13] Kuznetsov, I., Hess, S., Zakharov, A., Cipriani, F., Seran, E., Popel, S., Lisin, E., Petrov, O., Dolnikov, G., Lyash, A., and Kopin, S., "Numerical Modelling of the Luna-Glob Lander Electric Charging on the Lunar Surface with SPIS-DUST," *Planetary and Space Science*, Vol. 156, July 2018, pp. 62–70. https://doi.org/10.1016/j.pss.2018.03.004

[14] Chou, K., Wang, A., Yu, W., and Wang, J., "Laboratory Experiments on Dusty Spacesuit Charging and Arcing in Plasma," *IEEE Transactions on Plasma Science*, Vol. 47, No. 8, 2019, pp. 3898–3904. https://doi.org/10.1109/TPS.2019.2922243

[15] McKay, D. S., Heiken, G., Basu, A., Blanford, G., Simon, S., Reedy, R., French, B. M., and Papike, J., *Lunar Sourcebook: A User's Guide to the Moon*, Cambridge University Press, Cambridge, England, U.K., 1991, pp. 285–356, Chap. 7.

[16] Shkuratov, Y. G., and Bondarenko, N. V., "Regolith Layer Thickness Mapping of the Moon by Radar and Optical Data," *Icarus*, Vol. 149, No. 2, 2001, pp. 329–338. https://doi.org/10.1006/icar.2000.6545

[17] Borisov, N., and Mall, U., "Charging and Motion of Dust Grains near the Terminator of the Moon," *Planetary and Space Science*, Vol. 54, No. 6, 2006, pp. 572–580, http://www.sciencedirect.com/science/article/pii/S0032063306000092 [retrieved 1 Dec. 2022]. https://doi.org/10.1016/j.pss.2006.01.005

[18] Stubbs, T. J., Halekas, J. S., Farrell, W. M., and Vondrak, R. R., "Lunar Surface Charging: A Global Perspective Using Lunar Prospector Data," *Dust in Planetary Systems*, Vol. 643, Jan. 2007, pp. 181–184, http://adsabs.harvard.edu/abs/2007ESASP.643181S [retrieved 1 Dec. 2022].

[19] Farrell, W. M., Stubbs, T. J., Halekas, J. S., Delory, G. T., Collier, M. R., Vondrak, R. R., and Lin, R. P., "Loss of Solar Wind Plasma Neutrality and Affect on Surface Potentials near the Lunar Terminator and Shadowed Polar Regions," *Geophysical Research Letters*, Vol. 35, No. 5, 2008, Paper L05105. https://doi.org/10.1029/2007GL032653

[20] Poppe, A., and Horányi, M., "Simulations of the Photoelectron Sheath and Dust Levitation on the Lunar Surface," *Journal of Geophysical Research*, Vol. 115, No. A8, 2010, Paper A08106. https://doi.org/10.1029/2010JA015286

[21] Poppe, A., Halekas, J. S., and Horányi, M., "Negative Potentials Above the Day-Side Lunar Surface in the Terrestrial Plasma Sheet: Evidence of Non-Monotonic Potentials," *Geophysical Research Letters*, Vol. 38,

No. 2, 2011, Paper L02103.
https://doi.org/10.1029/2010GL046119
[22] Zimmerman, M., Farrell, W., Stubbs, T., Halekas, J., and Jackson, T., "Solar Wind Access to Lunar Polar Craters: Feedback Between Surface Charging and Plasma Expansion," *Geophysical Research Letters*, Vol. 38, No. 19, 2011, Paper L19202.
https://doi.org/10.1029/2011GL048880
[23] Poppe, A. R., Halekas, J. S., Delory, G. T., and Farrell, W. M., "Particle-in-Cell Simulations of Plasma Interaction with Lunar Crustal Magnetic Anomalies," *43rd Lunar and Planetary Science Conference*, Lunar and Planetary Institute (LPI), Houston, Texas, 2012, http://www.lpi.usra.edu/meetings/lpsc2012/ [retrieved 1 Dec. 2022].
[24] Fatemi, S., Holmström, M., and Futaana, Y., "The Effects of Lunar Surface Plasma Absorption and Solar Wind Temperature Anisotropies on the Solar Wind Proton Velocity Space Distributions in the Low-Altitude Lunar Plasma Wake," *Journal of Geophysical Research: Space Physics*, Vol. 117, No. A10, 2012, Paper A10105.
https://doi.org/10.1029/2011JA017353
[25] Poppe, A. R., Halekas, J. S., Delory, G. T., and Farrell, W. M., "Particle-in-Cell Simulations of the Solar Wind Interaction with Lunar Crustal Magnetic Anomalies: Magnetic Cusp Regions," *Journal of Geophysical Research*, Vol. 117, No. A9, 2012, Paper A09105.
https://doi.org/10.1029/2012JA017844
[26] Stubbs, T., Farrell, W., Halekas, J., Burchill, J., Collier, M., Zimmerman, M., Vondrak, R., Delory, G., and Pfaff, R., "Dependence of Lunar Surface Charging on Solar Wind Plasma Conditions and Solar Irradiation," *Planetary and Space Science*, Vol. 90, Jan. 2014, pp. 10–27, https://www.sciencedirect.com/science/article/pii/S0032063313001876 [retrieved 1 Dec. 2022].
https://doi.org/10.1016/j.pss.2013.07.008
[27] Deca, J., Divin, A., Lapenta, G., Lembège, B., Markidis, S., and Horányi, M., "Electromagnetic Particle-in-Cell Simulations of the Solar Wind Interaction with Lunar Magnetic Anomalies," *Physical Review Letters*, Vol. 112, No. 15, 2014, Paper 151102.
https://doi.org/10.1103/PhysRevLett.112.151102
[28] Han, D., Wang, J., and He, X., "Immersed Finite Element Particle-in-Cell Simulations of Plasma Charging at the Lunar Terminator," *Journal of Spacecraft and Rockets*, Vol. 55, No. 6, 2018, pp. 1490–1497.
https://doi.org/10.2514/1.A34002
[29] Han, D., He, X., Lund, D., and Zhang, X., "PIFE-PIC: Parallel Immersed Finite Element Particle-in-Cell for 3-D Kinetic Simulations of Plasma-Material Interactions," *SIAM Journal on Scientific Computing*, Vol. 43, No. 3, 2021, pp. C235–C257.
https://doi.org/10.1137/20M137344X
[30] Lund, D., He, X., Zhang, X., and Han, D., "Weak Scaling of the Parallel Immersed-Finite-Element Particle-in-Cell (PIFE-PIC) Framework with Lunar Plasma Charging Simulations," *Computational Particle Mechanics*, Vol. 9, No. 6, 2022, pp. 1279–1291.
https://doi.org/10.1007/s40571-022-00470-0
[31] Han, D., Wang, P., He, X., Lin, T., and Wang, J., "A 3D Immersed Finite Element Method with Non-Homogeneous Interface Flux Jump for Applications in Particle-in-Cell Simulations of Plasma-Lunar Surface Interactions," *Journal of Computational Physics*, Vol. 321, Sept. 2016, pp. 965–980.
https://doi.org/10.1016/j.jcp.2016.05.057
[32] Han, D., Wang, J., and He, X., "A Nonhomogeneous Immersed-Finite-Element Particle-in-Cell Method for Modeling Dielectric Surface Charging in Plasmas," *IEEE Transactions on Plasma Science*, Vol. 44, No. 8, 2016, pp. 1326–1332.
https://doi.org/10.1109/TPS.2016.2580698
[33] Li, Z., "The Immersed Interface Method Using a Finite Element Formulation," *Applied Numerical Mathematics*, Vol. 27, No. 3, 1998, pp. 253–267.
https://doi.org/10.1016/S0168-9274(98)00015-4
[34] Gong, Y., Li, B., and Li, Z., "Immersed-Interface Finite-Element Methods for Elliptic Interface Problems with Non-Homogeneous Jump Conditions," *SIAM Journal on Numerical Analysis*, Vol. 46, No. 3, 2008, pp. 472–495.
https://doi.org/10.1137/060666482
[35] Guzmán, J., Sánchez, M. A., and Sarkis, M., "Higher-Order Finite Element Methods for Elliptic Problems with Interfaces," *ESAIM: Mathematical Modelling and Numerical Analysis*, Vol. 50, No. 5, 2016, pp. 1561–1583.
https://doi.org/10.1051/m2an/2015093
[36] He, X.-M., "Bilinear Immersed Finite Elements for Interface Problems," Ph.D. Dissertation, Virginia Polytechnic Inst. and State Univ., Blacksburg, VA, 2009.
[37] He, X.-M., Lin, T., and Lin, Y., "Approximation Capability of a Bilinear Immersed Finite Element Space," *Numerical Methods for Partial Differential Equations: An International Journal*, Vol. 24, No. 5, 2008, pp. 1265–1300.
https://doi.org/10.1002/num.20318
[38] Li, Z., Lin, T., and Wu, X., "New Cartesian Grid Methods for Interface Problems Using the Finite Element Formulation," *Numerische Mathematik*, Vol. 96, No. 1, 2003, pp. 61–98.
https://doi.org/10.1007/s00211-003-0473-x
[39] Preusser, T., Rumpf, M., Sauter, S., and Schwen, L. O., "3D Composite Finite Elements for Elliptic Boundary Value Problems with Discontinuous Coefficients," *SIAM Journal on Scientific Computing*, Vol. 33, No. 5, 2011, pp. 2115–2143.
https://doi.org/10.1137/100791750
[40] Vallaghè, S., and Papadopoulo, T., "A Trilinear Immersed Finite Element Method for Solving the Electroencephalography Forward Problem," *SIAM Journal on Scientific Computing*, Vol. 32, No. 4, 2010, pp. 2379–2394.
[41] Guo, R., "Design, Analysis, and Application of Immersed Finite Element Methods," Ph.D. Dissertation, Virginia Polytechnic Inst. and State Univ., Blacksburg, VA, 2019.
[42] Zhang, X., "Nonconforming Immersed Finite Element Methods for Interface Problems," Ph.D. Dissertation, Virginia Polytechnic Inst. and State Univ., Blacksburg, VA, 2013.
[43] Feng, W., He, X.-M., Lin, Y., and Zhang, X., "Immersed Finite Element Method for Interface Problems with Algebraic Multigrid Solver," *Communications in Computational Physics*, Vol. 15, No. 4, 2014, pp. 1045–1067.
https://doi.org/10.4208/cicp.150313.171013
[44] He, X.-M., Lin, T., Lin, Y., and Zhang, X., "Immersed Finite Element Methods for Parabolic Equations with Moving Interface," *Methods for Partial Differential Equations: An International Journal*, Vol. 29, No. 2, 2013, pp. 619–646.
https://doi.org/10.1002/num.21722
[45] Adjerid, S., and Moon, K., "An Immersed Discontinuous Galerkin Method for Acoustic Wave Propagation in Inhomogeneous Media," *SIAM Journal on Scientific Computing*, Vol. 41, No. 1, 2019, pp. A139–A162.
https://doi.org/10.1137/16M1090934
[46] Adjerid, S., Lin, T., and Zhuang, Q., "Error Estimates for an Immersed Finite Element Method for Second Order Hyperbolic Equations in Inhomogeneous Media," *Journal of Scientific Computing*, Vol. 84, No. 2, 2020, p. 35.
https://doi.org/10.1007/s10915-020-01283-0
[47] Bai, J., Cao, Y., He, X.-M., Liu, H., and Yang, X., "Modeling and an Immersed Finite Element Method for an Interface Wave Equation," *Computers & Mathematics with Applications*, Vol. 76, No. 7, 2018, pp. 1625–1638.
[48] Adjerid, S., Chaabane, N., Lin, T., and Yue, P., "An Immersed Discontinuous Finite Element Method for the Stokes Problem with a Moving Interface," *Journal of Computational and Applied Mathematics*, Vol. 362, Dec. 2019, pp. 540–559.
https://doi.org/10.1016/j.cam.2018.07.033
[49] Jones, D., and Zhang, X., "A Class of Nonconforming Immersed Finite Element Methods for Stokes Interface Problems," *Journal of Computational and Applied Mathematics*, Vol. 392, Aug. 2021, Paper 113493.
https://doi.org/10.1016/j.cam.2021.113493
[50] Guo, R., and Lin, T., "A Higher Degree Immersed Finite Element Method Based on a Cauchy Extension for Elliptic Interface Problems," *SIAM Journal on Numerical Analysis*, Vol. 57, No. 4, 2019, pp. 1545–1573.
https://doi.org/10.1137/18M121318X
[51] He, X.-M., Lin, T., and Lin, Y., "The Convergence of the Bilinear and Linear Immersed Finite Element Solutions to Interface Problems," *Numerical Methods for Partial Differential Equations*, Vol. 28, No. 1, 2012, pp. 312–330.
https://doi.org/10.1002/num.20620
[52] Lin, T., Lin, Y., and Zhang, X., "Partially Penalized Immersed Finite Element Methods for Elliptic Interface Problems," *SIAM Journal on Numerical Analysis*, Vol. 53, No. 2, 2015, pp. 1121–1144.
[53] He, X.-M., Lin, T., and Lin, Y., "Interior Penalty Bilinear IFE Discontinuous Galerkin Methods for Elliptic Equations with Discontinuous Coefficient, Dedicated to David Russell's 70th Birthday," *Journal of Systems Science and Complexity*, Vol. 23, No. 3, 2010, pp. 467–483.
https://doi.org/10.1007/s11424-010-0141-z
[54] He, X.-M., Lin, T., and Lin, Y., "A Selective Immersed Discontinuous Galerkin Method for Elliptic Interface Problems," *Mathematical Methods in the Applied Sciences*, Vol. 37, No. 7, 2014, pp. 983–1002.
https://doi.org/10.1002/mma.2856

[55] Lin, T., Yang, Q., and Zhang, X., "A Priori Error Estimates for Some Discontinuous Galerkin Immersed Finite Element Methods," *Journal of Scientific Computing*, Vol. 65, No. 3, 2015b, pp. 875–894.

[56] Ewing, R. E., Li, Z., Lin, T., and Lin, Y., "The Immersed Finite Volume Element Methods for the Elliptic Interface Problems. Modelling '98 (Prague)," *Mathematics and Computers in Simulation*, Vol. 50, Nos. 1–4, 1999, pp. 63–76.
https://doi.org/10.1016/S0378-4754(99)00061-0

[57] Cao, W., Zhang, X., Zhang, Z., and Zou, Q., "Superconvergence of Immersed Finite Volume Methods for One-Dimensional Interface Problems," *Journal of Scientific Computing*, Vol. 73, Nos. 2–3, 2017, pp. 543–565.
https://doi.org/10.1007/s10915-017-0532-6

[58] He, X.-M., Lin, T., and Lin, Y., "A Bilinear Immersed Finite Volume Element Method for the Diffusion Equation with Discontinuous Coefficients, Dedicated to Richard E. Ewing on the Occasion of His 60th Birthday," *Communications in Computational Physics*, Vol. 6, No. 1, 2009, pp. 185–202.
https://doi.org/10.4208/cicp.2009.v6.p185

[59] Lin, T., Sheen, D., and Zhang, X., "A Nonconforming Immersed Finite Element Method for Elliptic Interface Problems," *Journal of Scientific Computing*, Vol. 79, No. 1, 2019, pp. 442–463.
https://doi.org/10.1007/s10915-018-0865-9

[60] Bai, J., Cao, Y., Chu, Y., and Zhang, X., "An Improved Immersed Finite Element Particle-in-Cell Method for Plasma Simulation," *Computers & Mathematics with Applications*, Vol. 75, No. 6, 2018, pp. 1887–1899.

[61] Bai, J., Cao, Y., He, X.-M., and Peng, E., "An Implicit Particle-in-Cell Model Based on Anisotropic Immersed-Finite-Element Method," *Computer Physics Communications*, Vol. 261, April 2021, Paper 107655.

[62] Cao, Y., Chu, Y., Zhang, X., and Zhang, X., "Immersed Finite Element Methods for Unbounded Interface Problems with Periodic Structures," *Journal of Computational and Applied Mathematics*, Vol. 307, Dec. 2016, pp. 72–81.
https://doi.org/10.1016/j.cam.2016.04.020

[63] Chu, Y., Cao, Y., He, X.-M., and Luo, M., "Asymptotic Boundary Conditions with Immersed Finite Elements for Interface Magnetostatic/Electrostatic Field Problems with Open Boundary," *Computer Physics Communications*, Vol. 182, No. 11, 2011, pp. 2331–2338.
https://doi.org/10.1016/j.cpc.2011.06.014

[64] Chu, Y., Han, D., Cao, Y., He, X.-M., and Wang, J., "An Immersed-Finite-Element Particle-in-Cell Simulation Tool for Plasma Surface Interaction," *International Journal of Numerical Analysis & Modeling*, Vol. 14, No. 2, 2017, pp. 175–200.

[65] Wang, J., He, X.-M., and Cao, Y., "Modeling Spacecraft Charging and Charged Dust Particle Interactions on Lunar Surface," *Proceedings of the 10th Spacecraft Charging Technology Conference*, 2007.

[66] Han, D., Wang, J., and He, X.-M., "Immersed-Finite-Element Particle-in-Cell Simulations of Plasma Charging at Lunar Terminator," *Journal of Spacecraft and Rockets*, Vol. 55, No. 6, 2018, pp. 1490–1497.

[67] Han, D., Wang, J., and He, X.-M., "A Non-Homogeneous Immersed-Finite-Element Particle-in-Cell Method for Modeling Dielectric Surface Charging in Plasmas," *IEEE Transactions on Plasma Science*, Vol. 44, No. 8, 2016, pp. 1326–1332.

[68] Depew, D., Han, D., Wang, J., He, X., and Lin, T., "Immersed Finite Element Particle-in-Cell Simulations of Lunar Surface Charging," *13th Spacecraft Charging Technology Conference*, Universities Space Research Assoc., SCTC 2014-199, Columbia, MD, 2014.

[69] Han, D., "Particle-in-Cell Simulations of Plasma Interactions with Asteroidal and Lunar Surfaces," Ph.D. Dissertation, Univ. of Southern California, Los Angeles, CA, 2015.

[70] Han, D., and Wang, J., "3-D Fully-Kinetic Particle-in-Cell Simulations of Small Asteroid Charging in the Solar Wind," *IEEE Transactions on Plasma Science*, Vol. 47, No. 8, 2019, pp. 3682–3688.
https://doi.org/10.1109/TPS.2019.2919895

[71] Yu, W., Han, D., and Wang, J., "Numerical Simulations of Dust Dynamics around Small Asteroids," *IEEE Transactions on Plasma Science*, Vol. 47, No. 8, 2019, pp. 3724–3730.
https://doi.org/10.1109/TPS.2019.2920263

[72] Yu, W., Wang, J. J., and Han, D., "Numerical Modeling of Dust Dynamics Around Small Asteroids," *AIAA SPACE Forum 2016*, AIAA Paper 2016-5447, 2016.

[73] Leahy, F. B., "Cross-Program Design Specification for Natural Environments (DSNE), Rev I," NASA SLS-SPEC-159, 2021.

[74] Heiken, G. H., Vaniman, D. T., and French, B. M., *Lunar Sourcebook: A User's Guide to the Moon*, Cambridge Univ. Press, Cambridge, England, U.K., 1991, pp. 61–79.

[75] "Moon Trek," NASA Jet Propulsion Lab., July 2018, https://trek.nasa.gov/moon/index.html [retrieved 15 July 2018].

[76] Halekas, J. S., Delory, G. T., Lin, R. P., Stubbs, T. J., and Farrell, W. M., "Lunar Surface Charging During Solar Energetic Particle Events: Measurement and Prediction," *Journal of Geophysical Research*, Vol. 114, No. A5, 2009, p. 5110.
https://doi.org/10.1029/2009JA014113

[77] Wang, J., and Hastings, D. E., "Ionospheric Plasma Flow over Large High-Voltage Space Platforms. II: The Formation and Structure of Plasma Wake," *Physics of Fluids B*, Vol. 4, No. 6, 1992, pp. 1615–1629.
https://doi.org/10.1063/1.860070

[78] Chou, K. L., "Experimental Investigation on Dusty Surface Charging in Plasma," Ph.D. Dissertation, Univ. of Southern California, Los Angeles, CA, Dec. 2017.

M. L. Walker
Associate Editor